npj | space exploration

Article

https://doi.org/10.1038/s44453-025-00015-8

Scarp-fronted deposits record the highest water level in Mars' Valles Marineris

Check for updates

I. Argadestya[1,2] ✉, F. Schlunegger[1], F. S. Anselmetti[1], A. Pommerol[2], A. Tullo[3] & N. Thomas[2]

We investigated the geomorphology of the promontory and the sedimentology of scarp-fronted deposits (SFDs) in Southeast Coprates Chasma using CTX, HiRISE, and CaSSIS images, and DEMs based on CaSSIS stereo pairs, HRSC and MOLA data. In the promontory, we find a network of branched channels bordered by screes and bedrock along the drainage divides, indicating a fluvial origin. The SFDs, occurring at the downstream end of the promontory, display convex break-in-slopes, separating a flat surface with a radial drainage network from a steep front downstream. We interpret these structures as records of fan-deltas with sources in the promontory, recording a sea-level high-stand. Notably, all identified SFDs occur at the same elevation range (-3750 to -3650 m) in Valles Marineris and the northern lowlands, and they were deposited between the Late Hesperian and the Early Amazonian. We consider this as the time with the largest availability of surface water on Mars.

Information on water-lain deposits on Mars provides a key contribution to the understanding of the planet's geologic history and its past environmental conditions, particularly considering the potential for past habitability. Consequently, major scientific efforts have been undertaken to reconstruct the geological history of Mars by documenting the occurrence of water[1–3]. For example, the northern lowlands of Mars, situated in the northern hemisphere of the planet, are considered to have hosted an at least 1.4 km-deep ocean[4]. In the same sense, the observation of hummocky-cross stratifications and trough cross-beds in Jezero[5] and Gale[6] Craters offered the basis to invoke the occurrence of turbidity currents induced by storms, again demonstrating the presence of a standing water body. Similarly, in the southern highlands, meandering incisions in Nili Fossae have been used to reconstruct the action of rivers eroding into bedrock[7]. Evidence of the availability of water, such as water-altered minerals[8–10] and geomorphic records of catastrophic floods[1], have also been reported for Valles Marineris, which is situated in the mid-latitudes and represents the largest canyon system on the planet[11] (Fig. 1A). This trough is located at 3°–15° S latitude and 260°–310° E longitude, and is over 4000 km long, 200 km wide, and reaches a depth of ca. −4700 m at its lowest point. The canyon itself is composed of interconnecting troughs (known as Chasmata), which are referred to as Ius, Ophir, Candor, Melas, and Coprates Chasma[12]. These individual troughs are connected with each other by the Valles Marineris Depression (VMD)[12]. The VMD itself is bordered to the North and to the South by the plateaus (Pl on Fig. 1B). In between the southern plateau and the VMD sits the promontory (Pr on Fig. 1B), which is a mountain range with a maximum elevation of ca. 1300 m. Valles Marineris is interpreted to have been generated through rifting driven by tensional stresses in response to magmatic activity. These mechanisms led to the rise of the Tharsis bulge during the Late Noachian to Early Hesperian[12–14], which in turn resulted in the formation of graben and collapse structures. Interestingly, at different locations along the interior wall of Valles Marineris, Morgan et al.[15] and Mondro et al.[16] reported the occurrence of what they referred to as Scarp-Fronted Deposits (SFDs). Similarly, Vaz et al.[17] described a type II fan of fluvio-deltaic origin in this setting. These authors considered such structures as evidence for a fan delta where rivers discharged their sedimentary bedloads into a standing water body. However, due to a lack of data resolving the topography at a high resolution, such as the more recently available 10 m-digital elevation models (DEMs) and orbital images (currently available with a spatial resolution of 0.5 m per pixel), the aforementioned authors were not able to assess the morphometric details of these structures, and most importantly to determine precisely the elevation of the inferred sea-level. Yet such information is crucial for reconstructing the spatial extension of the standing water body through mapping and for spatially correlating the various SFDs. Such data will then offer the basis to develop a scenario of how the inferred sea evolved through space and time, which is the goal of this paper.

Here, we benefit from high-resolution datasets collected by the CaSSIS[18], HiRISE[19], HRSC-MOLA[20], and CTX[21] instruments, focusing on the promontory of Southeast Coprates Chasma (Fig. 1A, B). We reconstruct the sedimentology and geomorphology of these structures at high resolution, which will allow us to determine precisely the elevation of the sea level, and to develop a scenario of how it evolved through time. Coprates Chasma, comprises a significant component of the extensive Valles Marineris canyon system[22]. Coprates Chasma extends approximately 1000 km in an east-west

[1]Institute of Geological Sciences and Oeschger Centre for Climate Change Research, University of Bern, Bern, Switzerland. [2]Institute of Physics, Space Research and Planetary Sciences Division, University of Bern, Bern, Switzerland. [3]INAF - Astronomical Observatory of Padova, Vicolo dell'Osservatorio, Padova, Italy. ✉e-mail: ignatius.indi@unibe.ch

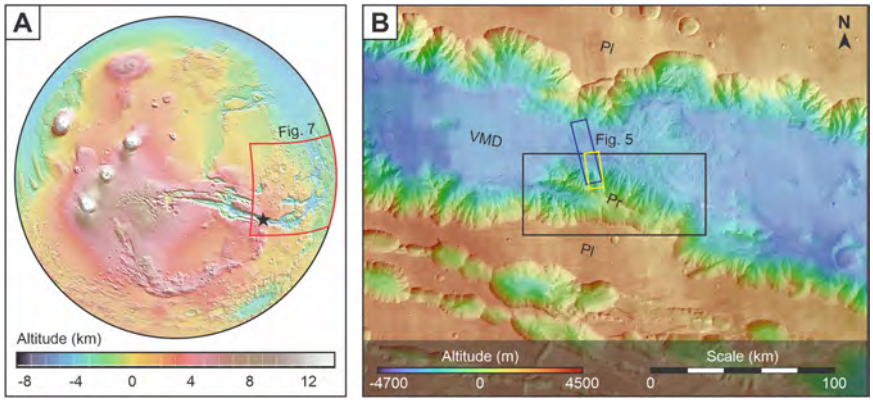

Fig. 1 | Map of Southeast Coprates Chasma's promontory. Location of the research area (indicated by * in (**A**) and by a black rectangle in (**B**) in Southeast Coprates Chasma. The red quadrangle (**a**) shows the extent of the identified SFDs. The dark blue and yellow rectangles (**B**) depict the areas for which HiRISE and CaSSIS images are available, respectively. Basemap image (**B**): Global CTX V1 overlain with MOLA – HRSC Global DEM V2. Pl= Plateau, Pr= Promontory, and VMD= Valles Marineris Depression.

direction, reaching up to 10 km in width and up to 8 km in depth. This large trough is connected to Melas Chasma to the west and to Capri and Eos Chasmata towards the east, forming an interconnected depression[23], which transitions into the Northern Lowlands (Fig. 1A). The target SFDs are situated in the southeastern part of Coprates Chasma (Fig. 1B). This trough was considered to have formed after the precursor ancestral basins were subjected to faulting episodes during Late Hesperian and Early Amazonian periods[22,24]. We proceed by describing the geomorphic and sedimentologic details of the SFD structures along the Southeast Coprates Chasma and tracing the lateral extent of the SFDs along the region. We find, for the first time, that these structures record the time (which we will place at the boundary between the Late Hesperian and the Early Amazonian) when the sea (or paleolake) on Mars reached the highest elevation at the scale of the entire planet.

Results

Morphometric properties of the promontory's drainage basins

The mountain belt to the south of the Valles Marineris' Coprates Chasma, which is referred to as the promontory (Figs. 1B and 2A) is surrounded by valley-floor deposits of the VMD in the northwest, and landslide material in the northeast. The promontory hosts multiple drainage basins with V-shaped cross-sectional geometries (ca. 19 valleys with a spacing of ~3.5 km and depths of incisions Δh ranging from 10 s of meters to more than 500 m), and thalwegs with decreasing elevations in the downstream directions. The largest of these drainage basins, referred to as basin A, has a catchment area of 74.68 km² and hosts an 11.31 km-long main channel along its thalweg, while the smallest, basin C, covers an area 3.91 km² and has a 2.64 km-long thalweg (Table 1). The elevations within these drainage basins range from −3343 to −35 m. In each basin, the thalwegs are represented by branched networks of channels. This is particularly visible in the upstream part of basin A, where this network has a Strahler stream order[25] of 3 (Fig. 3A), whereas the channel network of basins B and C have a Strahler order of 2 (Fig. 3A).

Geomorphic units in the southeast Coprates Chasma's Promontory

Mapping discloses the occurrence of three geomorphic architectural elements comprising (i) rugged ridges forming the drainage divides, (ii) smooth slopes that extend from the rugged ridges down to the thalwegs, and (iii) scarp fronted deposits (SFDs) with a well-visible apex at the downstream end of the thalwegs. The ridges themselves extend from the highest elevations of the promontory toward the downstream end of the valleys, and they compartmentalize the landscape into individual drainage basins in the promontory (Fig. 4A–C). The ridges have a rugged surface characterized by a zig-zag geometry with peaks and topographic saddles. Locally, the slopes are up to 35° steep. This geomorphic unit has a bright yellowish green color in the CaSSIS NIR-PAN-BLU (NPB) image (Fig. 5B). By referring to the visual appearance based on the roughness, smoothness, pattern, and structure visible through CTX (Fig. 4A) and HiRISE (Fig. 5V) images, the ridges appear to expose the bedrock forming the geological substrate of the drainage basins.

The second geomorphic element, characterized by its smooth surface on the CTX and HiRISE (Fig. 5iv) images, links the rugged ridges with the downstream thalwegs. It appears brightly teal colored on CaSSIS NPB images (Fig. 5B). We interpret these surfaces as scree deposits, which consist of the sedimentary material generated by weathering and erosion along the bedrock ridges. The third geomorphic elements are the SFDs that start with an apex, from where the deposits spread radially downstream, forming a fan-shaped geometry. These units end with scarp fronts at their distal terminations (Fig. 4A–C; 6), situated at an elevation of approximately −3700 m.

The elevation profile along the thalweg and the fan-shaped SFD A shows that the surface slope angle (α) gradually increases downstream from the apex to the valley floor. On the fan-shaped structure itself, the surface slope varies between 9.6° and 12.3°. The surface slope then increases to 27.2° at the front of the fan, defining a distinct break-in-slope (Fig. 4D; 6). The gradient then flattens as the topographic section approaches the bottom of Valles Marineris. Mapping shows that all three fan surfaces A, B and C exhibit similar radial extents, ranging from 2 to 2.5 km as measured from their respective apices. The availability of a high-resolution CaSSIS Stereo DEM for SFD A allows us to further specify the details of the inferred break-in-slope (Fig. 6). In particular, the boundary between the flat surface of the fan and the steep frontal part occurs consistently at an elevation of -3750 m (Table 1, Fig. 4A–C). In addition, a further break-in-slope appears to be visible at c. -3650 m and thus at a slightly higher elevation.

Sedimentary textures visible on HiRISE and CaSSIS images

Fan-shaped structure A, the reconstruction of which benefits from high spatial resolution imaging through the combination of CaSSIS and HiRISE datasets, displays a variety of surface features bearing information on its depositional history. In particular, dune ripples are present in both HiRISE and CaSSIS images (Fig. 5i, iii). These ripples, which appear as surficial bedforms with their lee sides oriented down-dip, overlay the preserved lobate shape of the fan surface. They are specifically found within the trough of the incised channel and are reflected in bright ocher color in the CaSSIS NPB image at the western side of the fan surface. Dune ripples that have formed along the channel's path overlay desiccation cracks as seen in HiRISE images (Fig. 5i, ii). The desiccation cracks occur mostly in the upper part of the fan surface and range in size from ~5 to 20 m (Fig. 5ii).

The extent of the SFD in Southeast Coprates Chasma

The identified scarp-fronted fan-shaped structures that we observed at an elevation range between −3750 and −3650 m (Figs. 4–6) in the promontory can be extended westward within Valles Marineris until the outflow channel leading to the northern dichotomy boundary (Fig. 7A). Tracking this elevation laterally revealed three additional lines of evidence for the occurrence

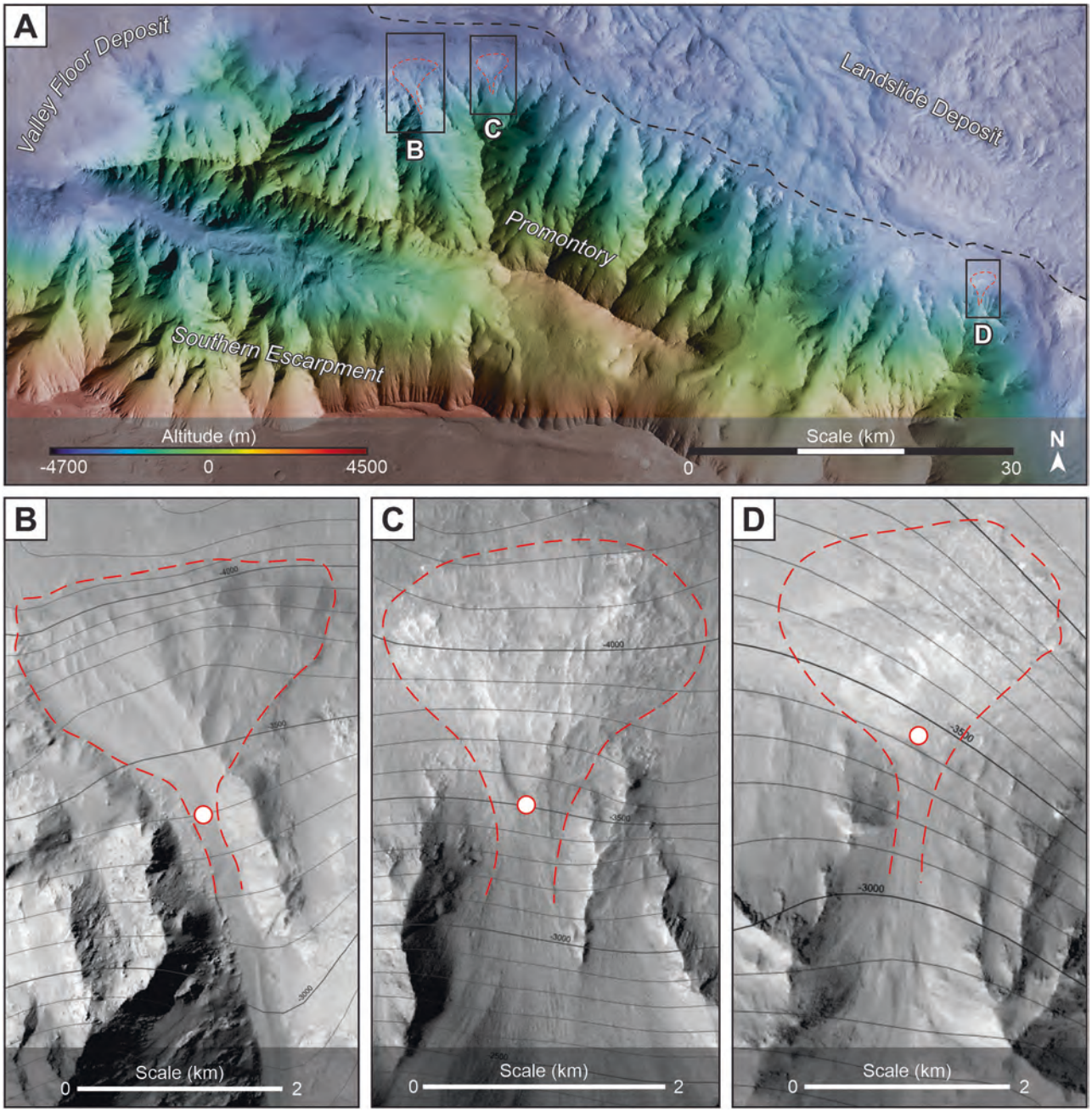

Fig. 2 | Scarp-Fronted Deposits (SFDs) in the promontory of Southeast Coprates Chasma. The CTX image overlain with MOLA – HRSC Global DEM in the research area (**A**) shows 3 SFDs (**B**-**D**) along the northern margin of the promontory in Southeast Coprates Chasma. The black dashed line defines the arcuate boundary of the landslide deposit (**A**). The red dashed line roughly illustrates the radial shape of the SFDs, and the white dots with red outline indicates their apices (**B**-**D**).

of scarp-fronted fan-shaped deposits (Fig. 7B–D). The first one is located ~500 km northeast of the fan-shaped structure on the promontory. It lies along the northern escarpment slope of Aurorae Sinus, at the outflow of Coprates Chasma, just before it transitions into the chaotic terrains of Eos Chasma and Capri Mensa. The material source of this SFD is situated in an incised valley. Its thalweg is oriented towards the SE. It then sharply descends into the valley floor depression containing chaotic mounds (Fig. 7B). Note that because of a lack of CaSSIS Stereo DEMs or any other high-resolution DEMs for these areas, we cannot further specify the elevation of the corresponding scarp fronts in these regions, but we find that the fronts do occur within the elevation range between -3750 and -3650 m.

The second scarp-fronted fan-shaped structure is situated in the West of Capri Chasma, just south of Innsbruck Crater (Fig. 7C). This SFD occurs at the escarpment in the transitory area between the Valles Marineris and Hydraotes–Chryse Chaos complex, two areas that are known to be the outwash downstream region of the entire valley depression before it reaches the northern lowlands dichotomy boundary[23,26]. This SFD was sourced from a drainage basin in the northeast. The feeding system flowed to the southwest where it created a sharp scarp-fronted topographic break. The frontal part then transitions into the valley depression, forming a steep slope. The third SFD is situated in the western escarpment of Hydraotes Chaos, where the valley floor contains abundant chaotic mounds (Fig. 7D). The general sediment-flow pathway in Valles Marineris is northeast–southwest, and southwest–northeast when it reaches Capri Chasma[23,27,28]. In the region of Hydraotes Chaos, the sediment pathway is oriented from the South to the North, as the VVMD transitions the Northern Ocean dichotomy boundary.

All additionally identified SFDs (Fig. 7B–D) are surrounded by ridges of exposed bedrock acting as drainage divides, similar to the ones in the

Table 1 | Drainage characteristics of the identified SFDs

Identified SFDs	Apex location		Channel length* (km)	Catchment area (km^2)	Mean slope of catchment (deg)*	Elevation of boundary between delta top – delta front (m)	Elevation of boundary between delta front and prodelta (m)***
	Lat	Lon					
SFD A	−13.588	−59.904	11.31	74.68	12.33	−3750 to −3650**	−4086
SFD B	−13.57	−59.8	3.43	11.71	15.77	c. −3700***	−4102
SFD C	−13.864	−59.112	2.64	3.91	12.09	c. -3700***	−4046

* Calculated for the segment between the upstream start of the thalweg to the apex.
** Taken from CaSSIS Stereo DEM.
*** Taken from HRSC-MOLA Global DEM.
The delta top – delta front boundary is interpreted as a paleoshoreline.

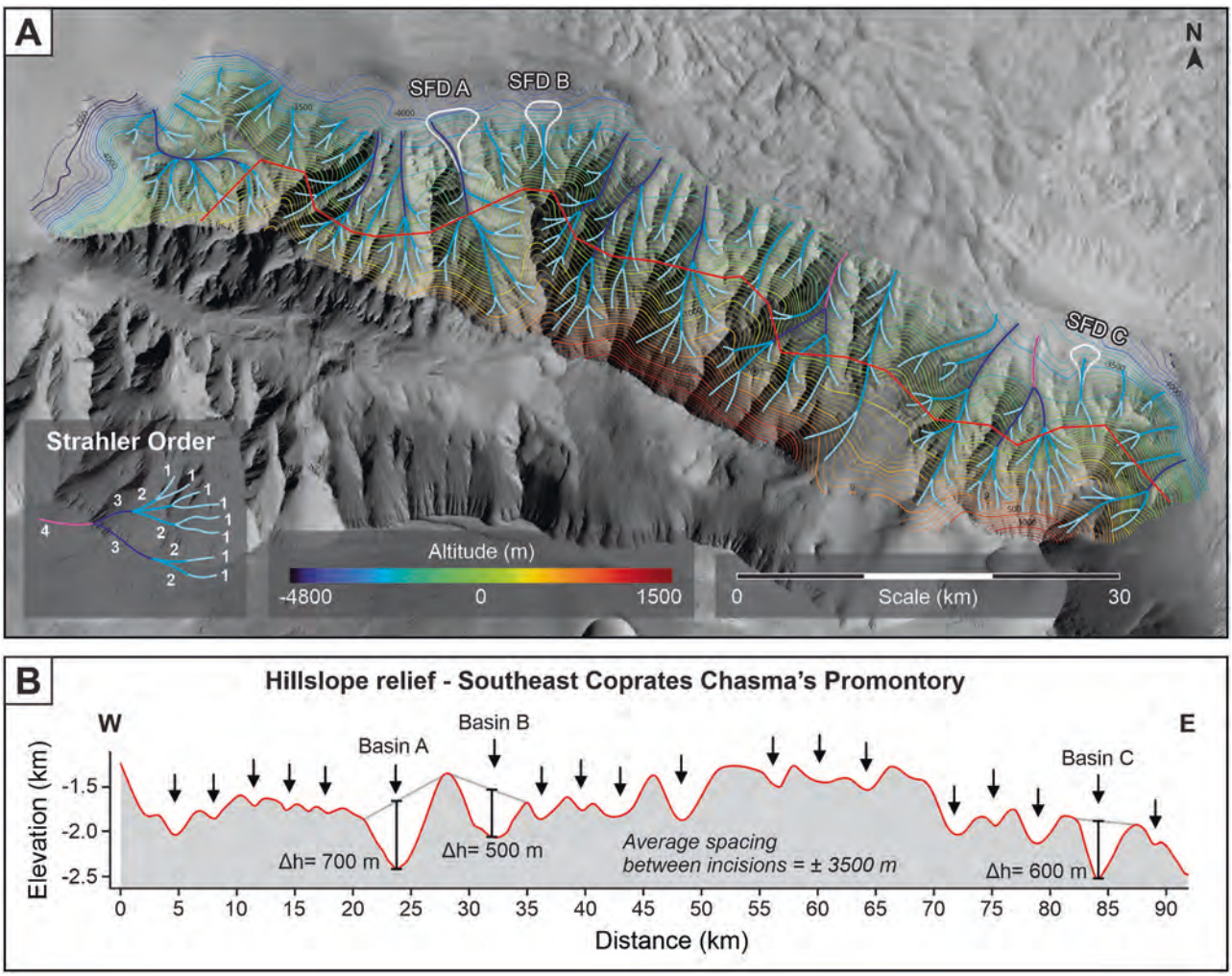

Fig. 3 | Morphometric properties of the Promontory's drainage basins. **A** Tributary channels identified in the northward facing promontory of the Southeast Coprates Chasma and Strahler orders characterizing the geometry of the channel networks in the various drainage basins. **B** Topographic cross-section drawn from elevation data that is extracted from the DEM along the red line across the promontory. The downward arrows indicate the depth of the local bedrock incision. SFD= scarp-fronted deposit.

Promontory of Southeast Coprates Chasma. All of them have drainage basins with exposed bedrock, scree deposits, and thalwegs, which grade into fan-shaped surfaces with a radial network of channels at their downstream outlets.

Discussion

In this section, we present geomorphic and sedimentologic evidence for arguing that the scarp frontal deposits (SFDs) in Coprates Chasma record the highest sea level on Mars, and that it occurred at the boundary between the Late Hesperian and the Early Amazonian, ca. 3.37 Ga ago. We proceed using a source-to-sink concept where we trace the routing of sedimentary particles from their origins to their deposition sites[29,30]. To this end, we first argue that the Promontory, which was the source area of the SFDs, was sculpted by fluvial erosion. This is followed by the second section where we reconstruct the geomorphic processes, including bedrock weathering, mass failure, and fluvial sediment transport. The transported material was stored

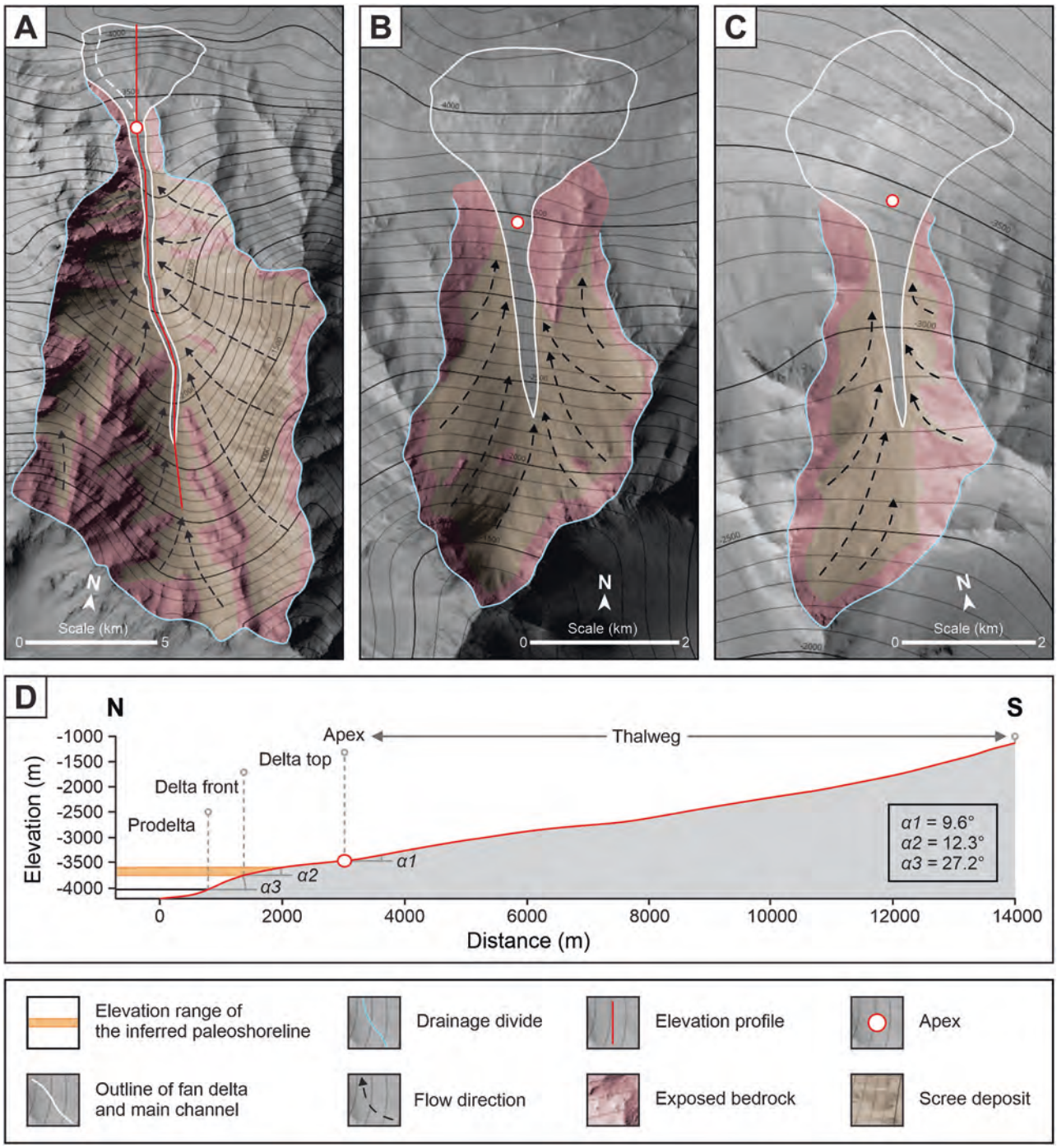

Fig. 4 | Geomorphological map of the SFDs and their drainage basins. **A** Illustrates SFD A, whereas **B** and **C** illustrate SFD B and SFD C, respectively. The white dashed line in SFD A (**A**) indicates the location where channel incision occurred. The profile illustrated on (**D**) displays a topographic cross-section of system A along the thalweg downstream to SFD A. The topographic data for drawing the cross-section is taken from the MOLA – HRSC Global DEM. The inferred elevation range of the paleoshoreline is drawn in orange. It is situated at the boundary between the delta top and the delta front at -3750 and -3650 m (see discussion).

on SFDs, which we will interpret—in the third section—as former fan deltas recording the elevation of the shoreline in the past. This inferred shoreline records the highest sea level on Mars at the boundary between the Late Hesperian and Early Amazonian as discussed in the last section based on the results of our mapping.

Here, we consider the circular-shaped geometries of the basins in the promontory of Coprates Chasma (Fig.3A) as characteristic features of a landscape that formed by fluvial and hillslope processes[31–33]. According to modeling studies[34,35], basins with such a shape are formed through headward retreat, where fluvial incision initiates at the downstream end of a topographic step, thereby forming a knickzone[35–37]. This step propagates towards the headwater area[34,35], thereby forming a network of branched channels at the bottom of V-shaped valleys[38–40]. Such branching is seen from CTX image by an increasing Strahler order in the downstream direction. In the case of a less-developed channel network, as is commonly found in smaller basins, the trunk stream will have a low Strahler order where it exits the drainage basin[34,41,42]. The result is a landscape with drainage basins of varying sizes, separated by drainage divides, hillslopes and a network of

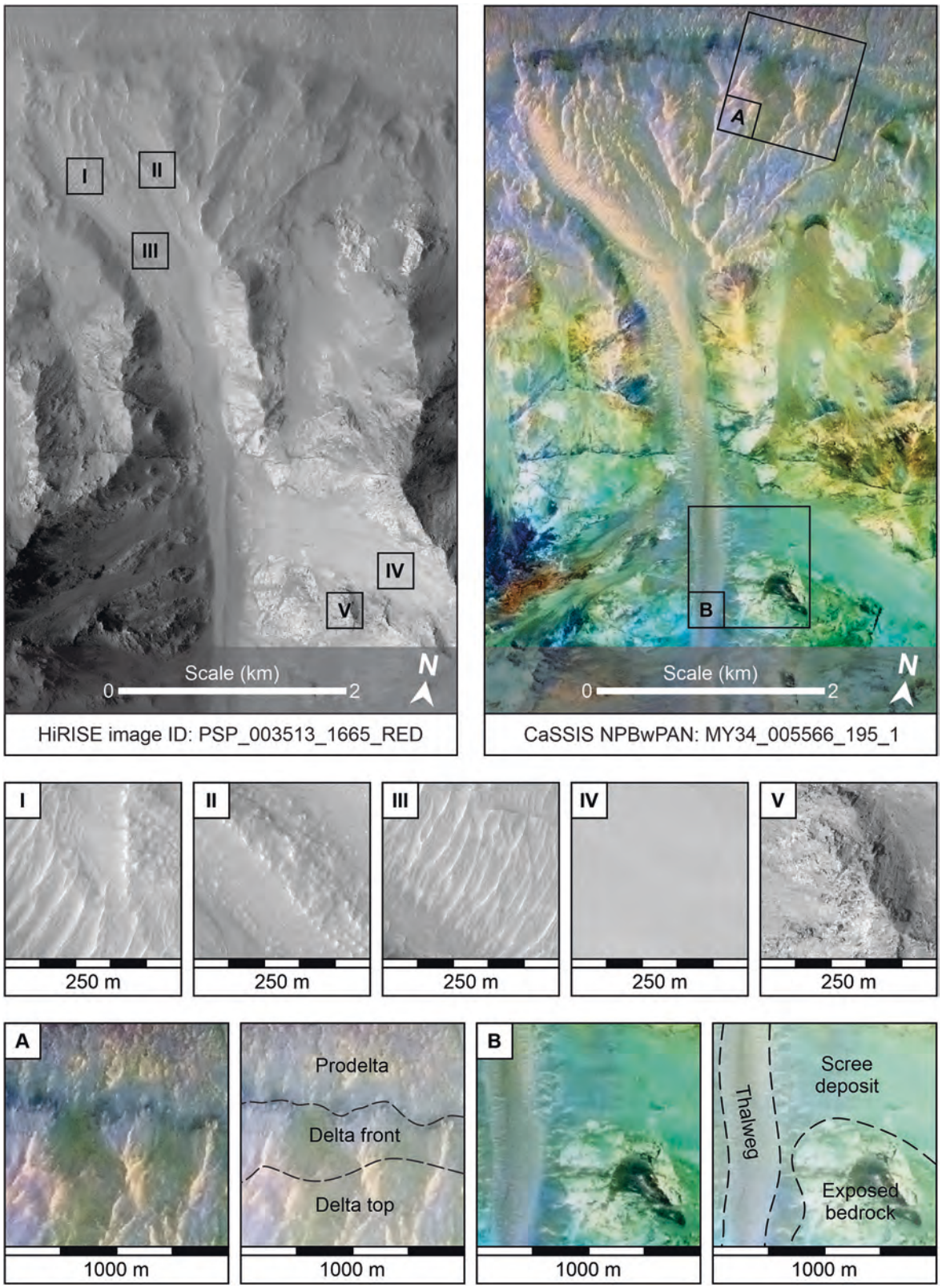

Fig. 5 | Sedimentary features on the surface of fan-shaped structure A through HiRISE and CaSSIS NPB images. Roman numerals mark the sedimentary textures detected through HiRISE. I: dunes overlying desiccation cracks, II: desiccation cracks, III: dune ripples, IV: scree deposit, V: exposed bedrock. Uninterpreted (**A**) and interpreted (**B**) CaSSIS subset images of the fan-shaped structure A along with the thalweg, scree deposit, and the exposed bedrock. Interpreted subset images are reduced by 35% in opacity to clarify the interpreted annotations.

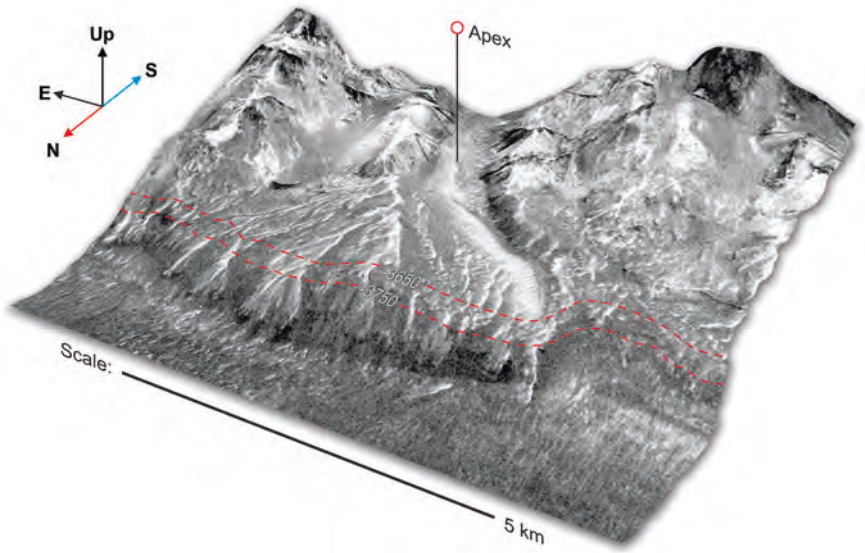

Fig. 6 | CaSSIS Stereo Pair DEM of SFD A. This figure illustrates an oblique 3D view of SFD A with -3750 and -3650m elevation contour (red dashed line), overlain on top of the scarp-fronted deposit. The surface is taken from CaSSIS PAN (Panchromatic) filter and the terrain elevation is taken from CaSSIS Stereo pair DEM (ID: MY34_005566_195_1).

channels that form the thalweg. The channels themselves define the local erosional base and operate as sedimentary conduits[43]. Note that we disregard the origin of the circular-shaped basins through groundwater sapping[44,45], because we do not see any evidence for upstream terminations of the valleys at pronounced headwalls[46].

The geomorphic properties of the promontory allow us to specify further the processes resulting in the generation of sedimentary material. In this context, we infer that the rims of the drainage divide likely expose the bedrock, where sediment was generated through weathering and rockfall. We base this interpretation on examples from Alpine-type landscapes where peaks and saddles along drainage divides have been mapped as exposed bedrock[47]. Farther downslope, the sedimentary material has been temporarily stored as screes on the hillslopes between the bedrock rim and the channel network. We see evidence for this interpretation[48,49], in the smooth texture of the surface, which itself mantles the bedrock. We acknowledge that upon comparing terrestrial and Martian landscapes, the lower gravitational acceleration on Mars most likely results in the deposition of larger grains on the hillslopes as the lower kinetic energy results in a lower fragmentation of the grains when they hit the ground during a rockfall[50]. The scree deposits were then evacuated towards the downstream end of the Promontory by fluvial transport, as evidenced by the geometry of the thalwegs (Fig. 4).

The SFDs at locations A, B and C, situated at the downstream end of the thalwegs, most likely record deposition on prograding fan deltas that occur at the margin of a standing water body, such as a lake or a sea[51]. In such systems, the feeding channels form the delta top[51] that spreads out radially from an apex, after which the bedload material becomes abruptly deposited forming a mouth bar. This feature defines a break-in-slope separating the relatively flat delta top (topsets) from the steeply dipping delta front (foresets)[52,53], thereby recording the elevation of the shoreline. We exclude the possibility where the SFDs would originally represent the deposits of alluvial fans spreading into a terrestrial basin, and where post-depositional erosion would have formed the topographic step. Such a mechanism would result in a break-in-slope that is linear and oriented perpendicularly to the paleoflow direction (e.g., downstream terminations of terrestrial fans in the Pisco valley, Peru[54]). In contrast, our SFDs have downstream convex terminations (Fig. 6), consistent with a fan-delta interpretation. Furthermore, the elevation of this break-in-slope records the highest level of the water in Valles Marineris because these deposits are not overlain by younger water-lain sediments[55]. In addition, the same elevation (c. −3700 m) of the break-in-slopes at fans A, B, and C indicates that these structures record the same water-level highstand and likely formed during the same period. We acknowledge that the high-resolution CaSSIS DEM allows identification of a higher break-in-slope situated at −3650 m. This could indicate that during the inferred highstand, the sea level was fluctuating in the range of c. 100 m, a pattern that is also observed on Earth[56,57]. A drop in the sea level could then explain the erosional depressions that are oriented parallel to the thalweg and occur on the topsets. In this context, (i) the limited depth of incision (several tens of meters), (ii) the presence of well-preserved desiccation cracks, and (iii) the occurrence of eolian dunes at the lateral margin of the channels (Fig. 5I) indicate that the feeding channels became completely dry during progressive sea-level lowering. Note that the outlets of the drainage basins between systems B and C are devoid of any preserved fan-delta structures, which we relate to post-depositional landsliding (Fig. 3A). Evidence for large-scale landsliding was already reported for the northern margin of Coprates Chasma, as evidenced by the occurrence of landslide deposits on the valley floor of Valles Marineris[58]. Similar processes can also explain the arcuate shape of the downstream boundary between drainage basins B and C, which could represent the escarpments of a landslide on the southern margin of this basin.

Fan-delta structures recording evidence for shorelines in the same elevation range as in Coprates Chasma are preserved in Capri Chasma, Chryse Chaos, and Hydraotes Chaos (Fig. 7). This indicates deposition during a period of a sea-level highstand extending from Valles Marineris to the Northern Lowland. In all these areas, no evidence for break-in-slopes at a higher elevation than the range between −3750 and −3650 m is found, suggesting that this was possibly the highest level reached by the sea. Our inferred coastal margin in this elevation range is supported by the occurrence of break-in-slopes in West Deuteronilus Mensae. Parker et al.[59] were able to map such structures on Viking images because they cast shadows on the landscape. Similar to our interpretation, Parker et al.[59] considered these break-in-slopes as evidence for a paleoshoreline. In addition, using data on the length of the shadows and considering the incidence angle at the time the images were taken, the aforementioned authors were also able to estimate the elevation of the inferred paleoshoreline, which agrees with our findings.

Here, we place the inferred sea-level highstand into a chronological context of the geomorphological evolution of Mars. The history of Valles Marineris started with the rifting during early Hesperian time[12–14], which created topographic steps with a throw of ~8 km between the valley floor at –5000 m, and a top of the promontory at ~1200 m. Channels that formed during the Early Hesperian time were one or two magnitudes narrower and shorter than fluvial incisions that formed between the Late Hesperian and the Early Amazonian[60–62]. This suggests that the drainage networks started to expand between the Early and the Late Hesperian, possibly establishing a fully fluvially controlled landscape on Mars[26,63,64]. We infer that the

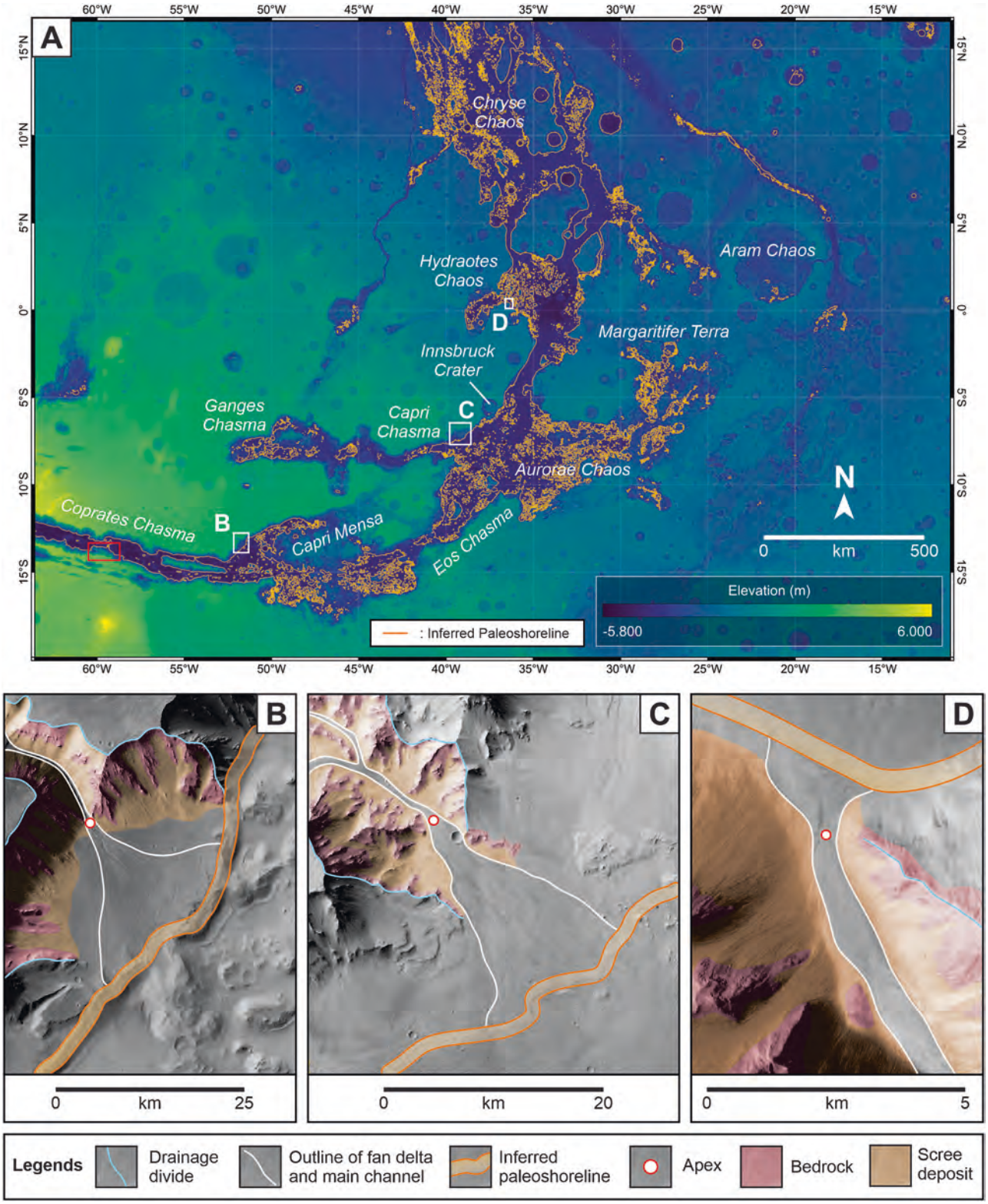

Fig. 7 | The extent of scarp-fronted deposits in Valles Marineris. A Westward extension of the inferred paleoshoreline (orange line) identified in the study area (red rectangle) across the Valles Marineris depression into Chryse Chaos, a transitory region between the Southern highlands and the Northern lowlands on Mars. The basemap images for (**B–D**) were acquired from Global CTX images. The DEM is taken from MOLA-HRSC Global Blend DEM V2.

landscape characterized by the V-shaped valleys occupied by networks of branched channels was also established during that time. The incipient topographic step, which formed during the period of rifting, in combination with a more humid climate resulted in effective fluvial erosion, the establishment of a dissected landscape in the Promontory, and the generation of clastic material[32,40,65,66]. This material then became deposited at the drainage basin outlets. Because our fan-delta deposits mark the highest sea level, we correlate the -3750 m shoreline with the boundary between the Late

Hesperian and the Early Amazonian. Sometime during the Early to Mid-Amazonian, when the water level started to fall, fluvial incision into previously deposited delta top sediment occurred. Finally, the late Amazonian marks the transition to a fully arid Mars[65], characterized by prevalent eolian activity[67,68], when gullies and fluvial channels began to be buried by dune ripples (Fig. 5i, iii).

In conclusion, the SFDs at the foothills of the Promontory of Southeast Coprates Chasma reflects a period (boundary between the Late Hesperian and the Early Amazonian) with the highest water availability on Mars. It resulted in the sedimentary accumulation, such as fan-delta deposits not only in Valles Marineris, but also in Capri Chasma, Hydraotes Chaos, and the Northern Ocean. This paleoshoreline is significant to establish the boundary condition for sedimentary realms between subaqueous and subaerial depositions, which will help the search for biosignatures on Mars, if they exist. Our research thus provides a further documentation of the time span where availability of liquid water on the surface was the highest during the evolution of this planet. We thus consider that our findings on the environmental stage during the Late Hesperian to Early Amazonian will have implications for research on the evidence for potential life on Mars.

Methods

Available data and image processing

We utilized existing geological maps of Coprates Chasma[69–71] to aid in the identification of fan-delta deposits in Southeast Coprates Chasma. High-resolution datasets from the Context Camera (CTX), DEM from Mars Express' High Resolution Stereo Camera (HRSC) and Mars Orbiter Laser Altimetry (MOLA), High-Resolution Imaging Science Experiment (HiRISE), and the Color and Stereo Surface Imaging System (CaSSIS) were used to analyze key surface features. Two CTX images covering the Southeast Coprates Chasma (E-060_N-16 and E-064_N-16) were merged in QGIS and subsequently cropped to fit the boundary of the research area. These data were processed using QGIS, an open-source geographic information system (GIS), enabling the integration of topographic and morphologic aspects to better understand the distribution and characteristics of fan-delta deposits within the region. The integration of different orbital imagery (CTX, HRSC-MOLA Global DEM, HiRISE, and CaSSIS) started with projecting them in the same coordinate reference system (CRS). Since the research area is situated at −13° latitude, we selected the IAU (International Astronomical Union) Standard Mars equidistant cylindrical projection (IAU 2015:49910). The QGIS plug-in *Mappy* was then used to create polygons of identified geomorphic units, which were saved in a shapefile (*.shp*) format.

The HiRISE image was stretched in the RED bands to optimize the brightness and contrast of the image. The CaSSIS image was processed by loading the CaSSIS cube file (*.cub*) in 3 bands of near infrared (NIR), panchromatic (PAN), and blue (BLU), producing the results of CaSSIS NPB images. These three bands were stretched with the *Standard Deviation Contrast Enhancement* function in QGIS with a mean value of ±3, and *whole raster* option for the *Statistic Extent*, rendered with the accuracy for an entire raster (*actual*). Both HiRISE and CaSSIS images were then georeferenced manually using the *GCPS Tie Raster Points* function under the *Georeferencer* utility toolbox in QGIS, with target basemap of CTX image, thus all orbital imageries were spatially superimposed in pixel-level precision.

Generation of a high-resolution DEM from CaSSIS stereo pairs

The CaSSIS DEM production is based on the principles of stereogrammetry and is conducted using the 3DPD pipeline[72]. In its most recent implementation, the 3DPD involves several steps aimed at providing an accurate surface reconstruction. This is accomplished through the use of *Bundle Adjustment* for the refinement of extrinsic parameters, including orbital positioning and pointing. The 3D surface is defined through a two-step process of stereogrammetric matching (sparse-to-dense), DEM interpolation, orthorectification of the original images, and post-processing[73]. The georeferencing and absolute elevation information are automatically aligned with the MOLA-HRSC hybrid data within the pipeline, prior to the interpolation phase, and has been further refined manually based on a level-4 HRSC Digital Elevation Model (ID: h1929_0000.da4.52.tif).

Geomorphic mapping

Mapping was performed based on a visual distinction between geomorphic elements at a scale of 1:10,000. Mapping was accomplished on DEMs with a vertical and lateral resolution of 10 m and 200 m, respectively and with an illumination from the NW. In this context, CTX images were used as a base map onto which the DEM information was projected. Further details about the occurrence of bedforms (such as wind ripples and desiccation cracks) were determined on the HiRISE image with a resolution of 0.5 m/px. Upon mapping, the geomorphic elements were delineated using information on brightness contrasts (visible on CTX images) and the surface textures as criteria (visible both on CTX and HIRISE images). This was accomplished using the contrasts in colors on the CaSSIS images. The geomorphic elements were finally differentiated using contrasts in illumination properties and smoothness patterns, break-in-slopes, and visible lineaments.

We mapped SFDs between Valles Marineris and the Northern Ocean on CTX images and the MOLA-HRSC Global DEM. The goal was to find further evidence for preserved paleoshorelines. We identified those features as SFDs that are characterized by (i) the occurrence of a well-visible and well-preserved break-in-slopes, (ii) a convex radial termination of the break-in-slopes (mentioned above) in the downstream direction, and (iii) that have a trunk channel that stretches into the headwaters farther upstream. We explored the entire region for such structures and mapped those that fulfilled all three criteria. We then registered the elevation (vertical resolution of 10 m) at which they occur.

Morphometric Calculation

The slope map was created using the input from MOLA-HRSC Global DEM V2, and processed using GDAL *Raster Analysis* in QGIS. We used Zevenbergen and Thorne formula to compute the angle in degree unit[74]. We localized the drainage analysis towards the northward-facing slope of Southeast Coprates Chasma Promontory. The DEM was clipped and given a new boundary. A Strahler-order classification in our localized DEM was then calculated. The delineation of channels was done manually following the contour line from the clipped DEM, and the channels were then marked accordingly to their Strahler order. For the Promontory, the topographic cross-section, which is oriented perpendicularly to the discharge direction, was produced with the *Elevation Profile* plugin in QGIS. The extracted data was then saved in *.csv* format to calculate the maximum depth of incision. Our source-to-sink approach using SFDs[59,75] differs from a previous study addressing computed valley-network morphologies to define extents of ancient seas[76].

Data availability

All datasets used in this research are free and openly accessible to the public. For this study, the CTX global mosaic produced by The Bruce Murray Laboratory for Planetary Visualization was used as the basemap imagery (retrieved from https://murray-lab.caltech.edu/CTX/). For the DEM, we used the MGS MOLA - MEX HRSC Blended DEM Global DEM V2 (retrieved from Planetary Data Science Annex, https://planetarymaps.usgs.gov/mosaic/Mars/HRSC_MOLA_Blend/Mars_HRSC_MOLA_BlendDEM_Global_200mp_v2.tif), and CaSSIS Stereo DEM (Stereo Image ID: MY34_005566_195_1), produced by INAF Astronomical Observatory of Padova. The HiRISE image (PSP_003513_1665) was retrieved from PDS directory (https://hirise-pds.lpl.arizona.edu/PDS/). The CaSSIS high-resolution color image (level 3 C, spatial resolution approximately 6 m/px) was accessed from CaSSIS Observations (https://observations.cassis.unibe.ch).

Received: 15 August 2025; Accepted: 18 October 2025;
Published online: 07 January 2026

References

1. Harrison, K. P. & Chapman, M. G. Evidence for ponding and catastrophic floods in central Valles Marineris, Mars. *Icarus* **198**, 351–364 (2008).
2. García-Arnay, Á & Gutiérrez, F. Reconstructing paleolakes in Nepenthes Mensae, Mars, using the distribution of putative deltas, coastal-like features, and terrestrial analogs. *Geomorphology* **359**, 107129 (2020).
3. Rivera-Hernández, F. & Palucis, M. C. Do deltas along the crustal dichotomy boundary of Mars in the Gale Crater Region record a Northern Ocean? *Geophys. Res. Lett.* **46**, 8689–8699 (2019).
4. Turbet, M. & Forget, F. The paradoxes of the Late Hesperian Mars ocean. *Sci. Rep.* **9**, 5717 (2019).
5. Edgar, L. A. et al. Shaler: in situ analysis of a fluvial sedimentary deposit on Mars. *Sedimentology* **65**, 96–122 (2018).
6. Heydari, E., Schroeder, J. F., Calef, F. J., Parker, T. J. & Fairén, A. G. Lacustrine sedimentation by powerful storm waves in Gale crater and its implications for a warming episode on Mars. *Sci. Rep.* **13**, 18715 (2023).
7. Fassett, C. I. & Head III, J. W. Fluvial sedimentary deposits on Mars: ancient deltas in a crater lake in the Nili Fossae region. *Geophys. Res. Lett*. **32**, 23456 (2005).
8. Chojnacki, M. & Hynek, B. M. Geological context of water-altered minerals in Valles Marineris, Mars. *J. Geophys. Res. Planets* **113**, 3070 (2008).
9. Fueten, F. et al. Interior layered deposits within a perched basin, southern Coprates Chasma, Mars: Evidence for their formation, alteration, and erosion. *J. Geophys. Res. Planets* **116**, 3695 (2011).
10. Carter, J., et al. A Mars orbital catalog of aqueous alteration signatures (MOCAAS). *Icarus* **389**, 115164 (2023).
11. Lucchitta, B. K. et al. The canyon system on Mars. 453–492 https://pubs.usgs.gov/publication/70200556 (1992).
12. Carr, M. H. & Head, J. W. Geologic history of Mars. *Earth Planet. Sci. Lett.* **294**, 185–203 (2010).
13. Andrews-Hanna, J. C. The formation of Valles Marineris: 1. Tectonic architecture and the relative roles of extension and subsidence. *J. Geophys. Res. Planets* **117**, 3953 (2012).
14. Mège, D., Cook, A. C., Garel, E., Lagabrielle, Y. & Cormier, M.-H. Volcanic rifting at Martian grabens. *J. Geophys. Res. Planets* **108**, 1852 (2003).
15. Morgan, A. M., Wilson, S. A. & Howard, A. D. The global distribution and morphologic characteristics of fan-shaped sedimentary landforms on Mars. *Icarus* **385**, 115137 (2022).
16. Mondro, C. A., Moersch, J. E. & Fedo, C. M. An updated global survey of alluvial fans on Mars: Distinguishing alluvial fans from other fan-shaped features through morphologic characterization. *Icarus* **389**, 115238 (2023).
17. Vaz, D. A., Di Achille, G., Hynek, B. M., Nelson, W. & Williams, R. M. E. Martian fan deposits: Insights on depositional processes and origin from mass balance survey. *Earth Planet. Sci. Lett.* **533**, 116049 (2020).
18. Thomas, N. et al. The colour and stereo surface imaging system (CaSSIS) for the ExoMars Trace Gas Orbiter. *Space Sci. Rev.* **212**, 1897–1944 (2017).
19. McEwen, A. S. et al. The high-resolution imaging science experiment (HiRISE) in the MRO extended science phases (2009–2023). *Icarus* **419**, 115795 (2024).
20. Gwinner, K. et al. The high resolution stereo camera (HRSC) of Mars Express and its approach to science analysis and mapping for Mars and its satellites. *Planet. Space Sci.* **126**, 93–138 (2016).
21. Dickson, J. L., Ehlmann, B. L., Kerber, L. & Fassett, C. I. The Global context camera (CTX) mosaic of mars: a product of information-preserving image data processing. *Earth Space Sci.* **11**, e2024EA003555 (2024).
22. Schultz, R. A. Multiple-process origin of Valles Marineris basins and troughs, Mars. *Planet. Space Sci.* **46**, 827–834 (1998).
23. Greeley, R., Kuzmin, R. O., Nelson, D. M. & Farmer, J. D. Eos Chasma, Mars: regional setting for a potential landing site for astrobiology. *J. Geophys. Res. Planets* **108**, 2014 (2003).
24. Lucchitta, B. K., Isbell, N. K. & Howington-Kraus, A. Topography of Valles Marineris: implications for erosional and structural history. *J. Geophys. Res. Planets* **99**, 3783–3798 (1994).
25. Strahler, A. N. Quantitative analysis of watershed geomorphology. *Eos Trans. Am. Geophys. Union* **38**, 913–920 (1957).
26. Howard, A. D., Moore, J. M. & Irwin III, R. P. An intense terminal epoch of widespread fluvial activity on early Mars: 1. Valley network incision and associated deposits. *J. Geophys. Res. Planets* **110**, 2459 (2005).
27. Walmsley, J., Fueten, F., Stesky, R., Hauber, E. & Rossi, A. P. Timing of smooth-topped chaotic terrain formation in southern Circum-Chryse. *Mars. Icarus* **441**, 116672 (2025).
28. Nummedal, D. & Prior, D. B. Generation of Martian chaos and channels by debris flows. *Icarus* **45**, 77–86 (1981).
29. Schlunegger, F. & Kissling, E. Slab load controls beneath the alps on the source-to-sink sedimentary pathways in the Molasse Basin. *Geosciences* **12**, 226 (2022).
30. Romans, B. W., Castelltort, S., Covault, J. A., Fildani, A. & Walsh, J. P. Environmental signal propagation in sedimentary systems across timescales. *Earth-Sci. Rev.* **153**, 7–29 (2016).
31. Li, M. et al. Global analysis of topographic and climatic controls on drainage basin shapes. *Geophys. Res. Lett.* **51**, e2023GL105804 (2024).
32. Tucker, G. E. & Slingerland, R. Drainage basin responses to climate change. *Water Resour. Res.* **33**, 2031–2047 (1997).
33. Chorley, R. J., Malm, D. E. G. & Pogorzelski, H. A. A new standard for estimating drainage basin shape. *Am. J. Sci.* **255**, 138–141 (1957).
34. Simpson, G. & Schlunegger, F. Topographic evolution and morphology of surfaces evolving in response to coupled fluvial and hillslope sediment transport. *J. Geophys. Res. Solid Earth* **108**, 2162 (2003).
35. Valla, P. G., van der Beek, P. A. & Lague, D. Fluvial incision into bedrock: Insights from morphometric analysis and numerical modeling of gorges incising glacial hanging valleys (Western Alps, France). *J. Geophys. Res. Earth Surf*. **115**, 1210 (2010).
36. Van den Berg, F., Schlunegger, F., Akçar, N. & Kubik, P. 10Be-derived assessment of accelerated erosion in a glacially conditioned inner gorge, Entlebuch, Central Alps of Switzerland. *Earth Surf. Process. Landf.* **37**, 1176–1188 (2012).
37. Schildgen, T. F. et al. Quantifying canyon incision and Andean Plateau surface uplift, southwest Peru: A thermochronometer and numerical modeling approach. *J. Geophys. Res. Earth Surf*. **114**, 1305 (2009).
38. Hack, J. T. Stream-profile analysis and stream-gradient index. *J. Res. US Geol. Surv.* **1**, 421–429 (1973).
39. Flint, J. J. Stream gradient as a function of order, magnitude, and discharge. *Water Resour. Res.* **10**, 969–973 (1974).
40. Schlunegger, F. & Norton, K. P. Headward retreat of streams in the Late Oligocene to Early Miocene Swiss Alps. *Sedimentology* **60**, 85–101 (2013).
41. Perron, J. T., Richardson, P. W., Ferrier, K. L. & Lapôtre, M. The root of branching river networks. *Nature* **492**, 100–103 (2012).
42. Allen, P. A. From landscapes into geological history. *Nature* **451**, 274–276 (2008).
43. Harvey, A. M. Effective timescales of coupling within fluvial systems. *Geomorphology* **44**, 175–201 (2002).
44. Salese, F., Pondrelli, M., Neeseman, A., Schmidt, G. & Ori, G. G. Geological Evidence of Planet-Wide Groundwater System on Mars. *J. Geophys. Res. Planets* **124**, 374–395 (2019).
45. Goldspiel, J. M. & Squyres, S. W. Groundwater Sapping and Valley Formation on Mars. *Icarus* **148**, 176–192 (2000).
46. Hoke, G. D., Isacks, B. L., Jordan, T. E. & Yu, J. S. Groundwater-sapping origin for the giant quebradas of northern Chile. *Geology* **32**, 605–608 (2004).
47. Delunel, R., van der Beek, P. A., Bourlès, D. L., Carcaillet, J. & Schlunegger, F. Transient sediment supply in a high-altitude Alpine environment evidenced through a 10Be budget of the Etages

catchment (French Western Alps). *Earth Surf. Process. Landf.* **39**, 890–899 (2014).
48. Savi, S., Delunel, R. & Schlunegger, F. Efficiency of frost-cracking processes through space and time: An example from the eastern Italian Alps. *Geomorphology* **232**, 248–260 (2015).
49. Nyberg, B. et al. Revisiting morphological relationships of modern source-to-sink segments as a first-order approach to scale ancient sedimentary systems. *Sediment. Geol.* **373**, 111–133 (2018).
50. Braat, L., Brückner, M. Z. M., Sefton-Nash, E. & Lamb, M. P. Gravity-Driven Differences in Fluvial Sediment Transport on Mars and Earth. *J. Geophys. Res. Planets* **129**, e2023JE007788 (2024).
51. Nichols, G. *Sedimentology and Stratigraphy*. (Wiley, 2023).
52. Fabbri, S. C. et al. A subaquatic moraine complex in overdeepened Lake Thun (Switzerland) unravelling the deglaciation history of the Aare Glacier. *Quat. Sci. Rev.* **187**, 62–79 (2018).
53. Ponce, J. J., Carmona, N., Jait, D., Cevallos, M. & Rojas, C. Sedimentological and ichnological characterization of delta front mouth bars in a river-dominated delta (Upper Cretaceous) from the La Anita Formation, Austral Basin, Argentina. *Sedimentology* **71**, 27–53 (2024).
54. Schlunegger, F., do Prado, A. H., Norton, K. P. & Delunel, R. On the mechanisms resulting in the formation of the Quaternary staircase terrace systems in the valleys of the western Andean margin of Peru. *Geomorphology* **442**, 108923 (2023).
55. Nienhuis, J. H. et al. River deltas and sea-level rise. *Annu. Rev. Earth Planet. Sci.* **51**, 79–104 (2023).
56. Haq, B. U., Hardenbol, J. & Vail, P. R. Chronology of fluctuating sea levels Since the Triassic. *Science* **235**, 1156–1167 (1987).
57. Miller, K. G. et al. The Phanerozoic record of global sea-level change. *Science* **310**, 1293–1298 (2005).
58. Chojnacki, M., Hynek, B., Black, S., Hoover, R. & Martin, J. *Geologic Mapping of the Coprates Chasma (MTM -15057), Mars: Year 2*. (USRA, 2016).
59. Parker, T. J., Stephen Saunders, R. & Schneeberger, D. M. Transitional morphology in West Deuteronilus Mensae, Mars: Implications for modification of the lowland/upland boundary. *Icarus* **82**, 111–145 (1989).
60. Howard, A. D. & Moore, J. M. Late Hesperian to early Amazonian midlatitude Martian valleys: Evidence from Newton and Gorgonum basins. *J. Geophys. Res. Planets* **116**, 3782 (2011).
61. Rodriguez, J. A. P. et al. Did the martian outflow channels mostly form during the Amazonian Period?. *Icarus* **257**, 387–395 (2015).
62. Leask, E. K. & Ehlmann, B. L. Evidence for deposition of chloride on Mars from small-volume surface water events into the Late Hesperian-Early Amazonian. *AGU Adv* **3**, e2021AV000534 (2022).
63. Mangold, N., Quantin, C., Ansan, V., Delacourt, C. & Allemand, P. Evidence for precipitation on Mars from dendritic valleys in the Valles Marineris Area. *Science* **305**, 78–81 (2004).
64. Fassett, C. I. & Head, J. W. The timing of martian valley network activity: constraints from buffered crater counting. *Icarus* **195**, 61–89 (2008).
65. Wordsworth, R. et al. A coupled model of episodic warming, oxidation and geochemical transitions on early Mars. *Nat. Geosci.* **14**, 127–132 (2021).
66. Limaye, A. B., Adler, J. B., Moodie, A. J., Whipple, K. X. & Howard, A. D. Effect of standing water on formation of fan-shaped sedimentary deposits at Hypanis Valles, Mars. *Geophys. Res. Lett.* **50**, e2022GL102367 (2023).
67. Diniega, S. et al. Modern Mars' geomorphological activity, driven by wind, frost, and gravity. *Geomorphology* **380**, 107627 (2021).
68. Chojnacki, M., Burr, D. M. & Moersch, J. E. Valles Marineris dune fields as compared with otherValles Marineris Depression martian populations: diversity of dune compositions, morphologies, and thermophysical properties. *Icarus* **230**, 96–142 (2014).
69. Witbeck, N. E., Tanaka, K. L. & Scott, D. H. *Geologic Map of the Valles Marineris Region, Mars*. *IMAP* https://pubs.usgs.gov/publication/i2010, https://doi.org/10.3133/i2010.(USGS, 1991)
70. Tanaka, K. L. et al. Geologic map of Mars: U.S. Geological Survey Scientific Investigations Map 3292. https://doi.org/10.3133/sim3292 (2014).
71. Chojnacki, M., et al. Global survey of paleo-bedforms on Mars. *Geomorphology* **466**, 109428 (2024).
72. Re, C., et al. Performance evaluation of 3DPD, the photogrammetric pipeline for the Cassis stereo images. *Int. Arch. Photogramm. Remote Sens. Spat. Inf. Sci.* **XLII-2-W13**, 1443–1449 (2019).
73. Tullo, A. et al. The generation of TGO-CaSSIS stereo products after six years of scientific mission: the complete stereo chain of INAF. *Int. Arch. Photogramm. Remote Sens. Spat. Inf. Sci.* **XLVIII-G-2025**, 1471–1476 (2025).
74. Zevenbergen, L. W. & Thorne, C. R. Quantitative analysis of land surface topography. *Earth Surf. Process. Landf.* **12**, 47–56 (1987).
75. Achille, G. D., Hynek, B. M. & Searls, M. L. Positive identification of lake strandlines in Shalbatana Vallis Mars. *Geophys. Res. Lett.* **36**, https://doi.org/10.1029/2009GL038854 (2009).
76. Luo, W. & Stepinski, T. F. Computer-generated global map of valley networks on Mars. *J. Geophys. Res. Planets* **114**, https://doi.org/10.1029/2009JE003357 (2009).

Acknowledgements

This work has been funded by the Swiss Federal Commission of Scholarships (FCS) through ESKAS (Bundes-Exzellenz-Stipendien), and within the framework of the National Center of Competence in Research PlanetS supported by the Swiss National Science Foundation under grant 51NF40_205606. The authors acknowledge the financial support of the SNSF. CaSSIS is a project of the University of Bern and funded through the Swiss Space Office via ESA's PRODEX program. The instrument hardware development was also supported by the Italian Space Agency (ASI) (ASI-INAF agreement no. 2020-17-HH.0), INAF / Astronomical Observatory of Padova, and the Space Research Center (CBK) in Warsaw.

Author contributions

I.A. initiated the research and wrote the main manuscript, including preparing all the figures; F.S. and F.S.A. helped with geomorphic analysis, surface processes interpretation, and morphometric calculation; A.T. helped with the production and processing of CaSSIS Stereo Pair DEM and related orthophotos; A.P. and N.T. helped with orbital imagery processing (CTX, HiRISE, and CaSSIS), interpretation, and methodology. N.T. is the Principal Investigator (PI), and N.T. is the co-PI of CaSSIS instrument on board of ESA's ExoMars Trace Gas Orbiter. All authors reviewed and approved the manuscript.

Competing interests

The authors declare no competing interests.

Additional information

Correspondence and requests for materials should be addressed to I. Argadestya.